Seasonal variation in sediment transport and deposition on a muddy clinoform in the Yellow Sea

Aimei Wang[a,b,c], David K. Ralston[c], Naishuang Bi[a,b], Zhen Cheng[c], Xiao Wu[a,b], Houjie Wang[a,b,*]

[a] College of Marine Geosciences/Key Laboratory of Submarine Geosciences and Prospecting Techniques, MOE, Ocean University of China, No. 238 Songling Rd., Qingdao, 266100, China
[b] Laboratory of Marine Geology, Qingdao National Laboratory of Marine Science and Technology, No. 1 Wenhai Rd., Qingdao, 266237, China
[c] Applied Ocean Physics and Engineering Department, Woods Hole Oceanographic Institution, Woods Hole, MA, 02543, USA

ARTICLE INFO

ABSTRACT

A calibrated, coupled model of the Bohai and Yellow Seas is developed to investigate sediment transport and deposition processes around a distinct clinoform east of the Shandong Peninsula. On the clinoform, deposition patterns vary seasonally with the regional hydrography and the East Asian Monsoon. A local maximum in sediment deposition is located offshore from spring to autumn, whereas sediment deposition is greater near the coast and decreases seaward in winter. From spring to autumn, a thermal front develops around the Yellow Sea Cold Water Mass and limits sediment transport seaward, enhancing sediment deposition and leading to high deposition rate in a focused region offshore. Sediment is transported to the region by the southward basin-scale cyclonic circulation, and the cross-shelf gradient in stratification, sediment resuspension, and vertical mixing at the front lead to a convergence in sediment transport and deposition. Sediment deposition over the clinoform is the greatest during the transition from summer to autumn when the thermal front persists but sediment supply increases. This results from weakened stratification and greater resuspension near the coast due to stronger winds, waves, and sea-surface cooling. A seasonal seaward shift of the frontal position toward deeper water is consistent with the decreasing heat flux, and the corresponding shift in location of maximum sediment deposition shifts seaward. In winter, the thermocline disappears and vertical mixing increases throughout the region. SSC over the clinoform increases due to active resuspension and net deposition decreases, and instead sediment is transported seaward and deposits in the South Yellow Sea. Current velocity, SSC and sediment deposition rates decrease seaward, in contrast to the focused trapping at the thermal front from spring to autumn. The deposition rates around the thermal front from spring to autumn are greater than in the winter, so the high net sediment accumulation over an annual cycle occurs in the same region as the longer-term accumulation preserved in the omega-shaped clinoform.

1. Introduction

Rivers are major connections between continents and global ocean, carrying freshwater, terrestrial sediment, organic material, and other natural elements to the sea (Milliman and Meade, 1983; Milliman and Syvitski, 1992). Sediment transport from rivers has formed not only large nearshore deltas but also distal muddy deposits on continental shelves, such as those adjacent to the Amazon River (Kuehl et al., 1986; Nittrouer et al., 1986, 1996), the Yellow River (Huanghe) (Alexander et al., 1991; Liu et al., 2002, 2004; 2007a; Yang and Liu, 2007), the Yangtze River (Changjiang) (Chen et al., 2000; Liu et al., 2006, 2007b; Xu et al., 2012) and the Mekong River (Liu et al., 2017).

In the 1980s, a prominent muddy deposit was observed in the northern Yellow Sea extending southward off the eastern Shandong Peninsula at 20–25 m water depth, some 350 km east of the present-day mouth of the Yellow River (Milliman et al., 1987). This clinoform has developed since 7 kyr B.P. (Li et al., 2014; Yang and Liu, 2007) and also extended along the northern side of the Shandong Peninsula (Liu et al., 2002, 2004). Based on high-resolution sub-bottom profiles, Yang and Liu (2007) identified the cross-shelf shape of this clinoform, largely different from the classic sigmoidal-shaped, seaward prograding sequence. This distal clinoform instead was a bidirectional-dipping (landward and seaward), convex sedimentary feature, and so was described as omega-shaped ('Ω'). The thickest part of this clinoform (~40 m) is located at ~50 km away from the coast and the clinoform thickness decreases in both landward and seaward directions. Previous

---

sedimentary studies suggested that this Shandong Subaqueous Delta represented a direct escape route of Yellow River sediment into the South Yellow Sea (Alexander et al., 1991; Bian et al., 2013a; Qiao et al., 2016). Records of heavy metals and anthropogenic arsenic also indicated that sediment preserved in the clinoform off the Shandong Peninsula was mostly derived from the Yellow River and Bohai Sea (Xu et al., 2016).

The lines of evidence from various studies consistently point to the Yellow River as the sediment source for the muddy clinoform, but large uncertainty still remains in the mechanisms of its formation. Early interpretations of the clinoform shape mainly focused on the role of the postglacial sea-level rise in controlling the along-shelf clinoform formation, particularly the rapid sea-level rise associated with the meltwater pulse 1b (MWP-1b) at 11 ka BP, and on the impacts from the channel migrations of the lower Yellow River (Liu et al., 2002, 2004, 2007a). Yang and Liu (2007) ascribed the development of the clinoform to weak bottom shear stress in a less-energetic environment and to the regional circulation pattern. Tides might significantly influence the regional circulation such as the strength of the Yellow Sea Warm Current and the associated cyclonic gyre (Lu et al., 2011; Ren et al., 2014) by influencing the thermal front development (Zhao, 1985; Ren et al., 2014; Zang et al., 2017). This thermal front represents a baroclinic pressure gradient that affects the general circulation patterns. For example, Lu et al. (2011) proposed that the strength of the basin-scale cyclonic gyre in the Yellow Sea is influenced by the thermal front, which depends on tidal mixing. The sediment distribution is also closely related to the strength of the tidal current (Chen and Zhu, 2012).

Based on observations and modeling of circulation in the winter season, Wang et al. (2013) speculated that sediment mainly deposits in summer due to constraints by a thermal front and stratification. They also suggested that weaker currents at the interface between the Yellow Sea Coastal Current and Yellow Sea Warm Current favor the rapid deposition and formation of the muddy clinoform. Based on seasonal shipboard measurements and physical fields extracted from the global Hybrid Coordinate Ocean Model (HyCOM), Zang et al. (2017) suggested that in winter, a thermal front seaward of the Shandong Peninsula and a nearshore mixing front play critical roles in the formation of the mud patch. Both Wang et al. (2013) and Zang et al. (2017) suggested that the thermal front could promote the formation of the omega-shaped clinoform, but their hypotheses were based on limited observations of SSC and temperature, and did not account for longer-term variation of SSC and temperature, nor did they directly measure sediment deposition rates.

This study provides new model results that characterize the hydrodynamics, sediment transport, and sediment deposition in the vicinity of the thermal front at seasonal to annual scales. We develop a high-resolution and longer-term coupled model (including current, waves and sediment) of the Bohai and Yellow Sea in combination with in-situ observations. We use the calibrated model results to examine the mechanisms of sediment transport and the seasonal characteristics that impact sediment deposition around a muddy clinoform.

2. Regional setting

The Yellow Sea is a shallow and semi-enclosed marginal sea bordered by China and the Korean Peninsula, and is connected with the Bohai Sea to the north and the East China Sea to the south (Fig. 1a). The average water depth of the Yellow Sea is 44 m, with a shallow region along the Chinese coast, a NW-SE trough (Yellow Sea trough) defined by the ~80 m isobath in the middle, and a steep, narrow shelf along the Korean coast.

Tides in the Yellow Sea are mixed diurnal/semidiurnal (Naimie et al., 2001). M_2 is the dominant tidal constituent, followed by S_2 and K_1 (Teague et al., 1998). The tidal range is the greatest along the west coast of Korea (~3.5 m) and Chinese coast (~3.0 m) (Choi et al., 2003). The M_2 currents along the western coast of Korea are

~60–80 cm s^{-1}, generally decrease to 20–40 cm s^{-1} along the coast of China except near the Yangtze River Estuary, where tidal currents can be 100 cm s^{-1} (Bao et al., 2001; Fang, 1986).

The hydrography of the Yellow Sea is strongly affected by seasonally varying atmospheric conditions such as heating, cooling and wind stress, and in particular by the East Asian Monsoon. During the winter, strong northerly or northwesterly winds generally prevail over the Yellow Sea, while the summer is characterized by weak southerly winds (Naimie et al., 2001; Wang et al., 2014b). Due to the dominance of the East Asian Monsoon, the southward-propagating waves produced by the strong northerly winds are dominant in the winter with an averaged significant wave height of 0.9–1.9 m, whereas in summer the northward-propagating waves are much weaker (Su and Yuan, 2005; Chen et al., 2016). The seasonally varying winds and waves lead to distinct seasonality in the hydrographic structure (Naimie et al., 2001), SSC distribution (Wang et al., 2014b; Zang et al., 2017), and sediment-transport patterns (Bi et al., 2011; Wang et al., 2016).

The steady circulation patterns in the Yellow Sea are dominated by the Yellow Sea Warm Current (Fig. 1) in winter, which flows northward along the western side of the Yellow Sea trough. The Yellow Sea Coastal Current (Fig. 1.) flows southward along the western edge of the basin (Isobe, 2008; Lie and Cho, 1994), intersects with northward current around 32.5–34°N, turns seaward in the vicinity of the Old Yellow River Delta (Wu et al., 2018). The Yellow Sea Warm Current is generally enhanced in winter when strong northerly winds are dominant over the Yellow Sea (Hsueh, 1988; Riedlinger and Jacobs, 2000; Teague and Jacobs, 2000). The northerly winds drive cold coastal water flowing southward, importing warmer, and more saline water on the western slope of Yellow Sea trough (Lie et al., 2009; Lin and Yang, 2011; Qu et al., 2018) and forming a strong velocity shear that has been previously documented by observations, simulations, and satellite data (Hickox et al., 2000; Ma et al., 2006; Tana et al., 2017; Wang and Liu, 2009).

Another important hydrographic feature is the Yellow Sea Cold Water Mass, which is the cold water below the seasonal thermocline from spring through autumn (Fig. 1a). The Yellow Sea Cold Water Mass has been interpreted to be nearly motionless during summer (Li and Yuan, 1992). However, recent studies (Park, 1986; Moon et al., 2009; Wang et al., 2014a; Xu et al., 2003; Zhang et al., 2008; Pang et al., 2004) suggested that in the northeast this cold-water mass is displaced southward from the northern to the central Yellow Sea during summer. Previous numerical models and observations have suggested that the summer circulation of Yellow Sea Cold Water Mass in the central part of the Yellow Sea is cyclonic basin-scale (Beardsley et al., 1992; Pang et al., 2004; Xia et al., 2006) (Fig. 1a). Due to the warm air temperature, strong downward net radiation, and strong tidal mixing, a bottom thermal front forms along the boundary of the Yellow Sea Cold Water Mass (Moon et al., 2009; Xia et al., 2006; Zhao, 1985), whereas surface thermal fronts are less prevalent (Hickox et al., 2000).

Due to variations in physical processes (e.g., wind, current, wave, hydrographic structure) (Choi et al., 2003; Chu et al., 1997; Naimie et al., 2001), patterns of SSC, sediment transport and deposition in the Yellow Sea have strong seasonal and spatial variations. Studies have found greater sediment flux in winter than in summer, and the large values of SSC were identified at the east side of the Shandong Peninsula, off the Old Yellow River Delta and outside the Yangtze River Estuary (Zang et al., 2017; Bian et al., 2013b; Lee and Chough, 1989; Luo et al., 2017). To better understand how seasonal patterns may relate to longer-term sediment-transport and deposition in the Yellow Sea, we use a high-resolution model to capture seasonal variation in the currents, hydrography, sediment transport, and sediment deposition.

3. Model set-up

The Coupled Ocean-Atmosphere-Wave-Sediment Transport (COAWST, Warner et al., 2008; 2010) Modeling System combines
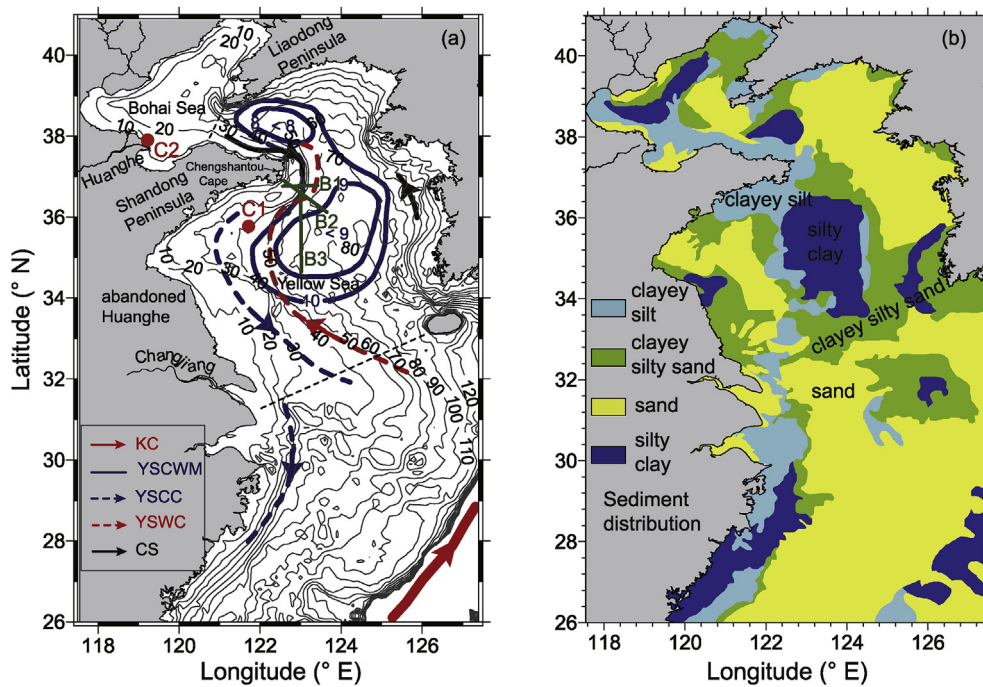
Fig. 1. (a) Topography and circulation pattern of the Bohai and Yellow Seas: Yellow Sea Cold Water Mass (YSCWM, 10 °C), Kuroshio Current (KC), Yellow Sea Coastal Current in winter (YSCC), Yellow Sea Warm Current (YSWC), Current in Summer (CS) (after Naimie et al., 2001; Lu et al., 2011; Zhang et al., 2008) and (b) median grain-size distribution of seabed sediment (Li et al., 2005; Wang et al., 2012). (For interpretation of the references to color in this figure legend, the reader is referred to the Web version of this article.)

several state-of-the-art modeling components, including the Regional Ocean Modeling System (ROMS, Shchepetkin and McWilliams, 2005) for ocean circulation, Simulating Waves Nearshore (SWAN, Booij et al., 1999) for waves and the Community Sediment Transport Modeling System (CSTMS, Warner et al., 2008) for sediment transport. The models are coupled via the Model Coupling Toolkit (MCT, Jacob et al., 2005; Larson et al., 2005). ROMS and SWAN are two-way coupled, with SWAN sending wave information to ROMS, including arrays of wave height, wavelength, average wave period at the surface and near the bottom, wave-propagation direction, near-bottom orbital velocity, and wave-energy dissipation rate. ROMS passes the array of water depth, sea-surface elevation, and current velocity to SWAN.

To reduce the influence of open boundary conditions, the model domain is expanded to cover the Bohai Sea, the Yellow Sea and the East China Sea (26°–41°N, 117.5°–127.5°E) (Fig. 1a). The horizontal resolution is 1.5′ × 1.5′ with 30 uniform layers in vertical dimension. The model bathymetry is interpolated from the 1.0′ × 1.0′ resolution topography data of Laboratory for Coastal and Ocean Dynamics Studies, Sung Kyun Kwan University, Korea (Bian et al., 2013a). The minimum depth is set to 3 m in the Bohai Sea and 4 m in the rest of model domain, and the maximum water depth is 2500 m. A robust HSIMT-TVD advection scheme (Wu and Zhu, 2010) is used to solve the advection term and k-ω turbulence closure model is implemented to parameterize the vertical mixing (for details see Warner et al., 2005). The surface forcing is calculated based on bulk flux formulae (Fairall et al., 2003; Oost et al., 2002; Taylor and Yelland, 2001) and the atmospheric forcing data are interpolated from European Center for Medium-Range Weather Forecasts (ECMWF, https://www.ecmwf.int) with 0.125° spatial resolution, including dataset of wind, mean sea-level pressure, air temperature, relative humidity, precipitation and net solar shortwave radiation as averages every 6 h. Eight major tidal constituents (M_2, S_2, N_2, K_2, K_1, O_1, P_1 and Q_1) derived from the OSU TOPEX/Poseidon Global Inverse Solution (Egbert et al., 1994; Egbert and Erofeeva, 2002) are used as tidal forcing at the open boundary. HYCOM + NCODA Global 1/12° Analysis (GLBa0.08/expt_91.2) data are used to define sea-level, temperature, salinity and currents at the two open boundaries (south

and east) and to create the initial conditions.

The SWAN model uses the same horizontal grid and bathymetry as ROMS. The wave model is driven by the 3-h wind from ECMWF. At the open ocean boundary, the peak wave period, average wave direction at the peak period, and significant wave height are interpolated from the Wave-Watch III products (http://polar.ncep.noaa.gov/waves/index2.shtml). Coupled model variables are exchanged between SWAN and ROMS every hour.

In the sediment module, three particle classes are defined (clay, silt, and sand), and the initial condition for seabed composition is established using four characteristic bottom types composed of different fractions for the particle classes (sand, clayey silty sand, clayey silt, silty clay). The particle-size class characteristics and initial bed sediment conditions are listed in Table 1. The particle parameters follow Bian et al. (2013a), but the settling velocity of the clay (increased to $0.2\,\text{mm s}^{-1}$ from $0.1\,\text{mm s}^{-1}$) and the surface erosion rate (increased to $4\times10^{-5}\,\text{kg m}^{-2}\,\text{s}^{-1}$ from $2\times10^{-5}\,\text{kg m}^{-2}\,\text{s}^{-1}$) are adjusted based on comparisons with observations of SSC. The spatial distribution of bed-

Table 1
Parameters for modeling of sediment transport and intial sediment composition of seabed.

	Clay	Silt	Sand	
Diameter (mm)	0.0039	0.016	0.256	
Settling velocity (mm s^{-1})	0.2	0.4	15.3	
Critical shear stress (N m^{-2})	0.02	0.07	0.16	
Density (kg m^{-3})	2650	2650	2650	
Surface erosion rate (kg m^{-2} s^{-1})	0.00004	0.00004	0.00004	
Porosity	0.4	0.4	0.4	

	Clay	Silt	Sand	Mean grain diameter (mm)
Sand	5%	20%	75%	0.12
Clayey silty sand	33%	33%	33%	0.025
Clayey silt	25%	65%	10%	0.015
Silty clay	40%	50%	10%	0.012

sediment conditions (Fig. 1 (b)) is based on Li et al. (2005) and Wang et al. (2012). The initial fractions of the particle classes are from Yuan (2015). Two bed layers are used, with initial thicknesses 0.2 m (upper layer) and 10 m (lower layer) as in Bian et al. (2013a). Currents and Waves perform the major roles in sediment suspension in near-coastal area (Wang et al., 2011), here currents and waves are both considered. In the model, the wave-current BBL model (ssw_bbl) of Madsen (1994) is implemented to calculate the bottom shear stress under the influence of wave-current interaction (for details see Warner et al., 2008).

The Yellow River and Yangtze River are the two dominant sources for freshwater and sediment input to the Bohai Sea, the Yellow Sea, and the East China Sea (Wang et al., 2014b; Zeng et al., 2015). Historically, their freshwater discharges accounted for ∼4% and ∼80% of the total riverine inputs, whereas their sediment discharges accounted for ∼65% and ∼30%, respectively (Ichikawa and Beardsley, 2002; Liu et al., 2013; Xu et al., 2009; Yang et al., 2003). Sediment discharges from the Yellow River and Yangtze River have been sharply reduced in recent decades, and for example in 2012 their respective sediment discharges represented ∼48% and ∼43% of the total inputs. (Yellow River: 0.18×10^9 metric tons; Yangtze River: 0.16×10^9 metric tons. Data are from Bulletin of Chinese River Sediment, available at http://www.mwr.gov.cn/sj/tjgb/zghlnsgb/). At present, input from smaller Chinese rivers and Korean rivers is less than 30×10^6 metric tons (Yang et al., 2003).

The Yellow River runoff and sediment discharge are from observed daily records at station Lijin (∼100 km upstream of Yellow River mouth) and Yangtze River data are interpolated from observed monthly records of station Datong (∼500 km upstream of Yangtze River). Following Li et al. (2005) and Zeng et al. (2015), to account for the difference between gauging stations and river mouths, the sediment discharge at the river mouths is set to be 70% of their upstream gauge observations, but the water discharge is kept unchanged. The fraction of clay, silt and sand are set at 20%, 70% and 10% for the Yellow River and 33.3% each for the Yangtze River. The baroclinic time step is 30 s with 120 barotropic time-steps between each baroclinic time step. The simulation runs from 1 December 2011 to 1 February 2013 (14 months) to allow comparison with available observations.

The muddy clinoform at east of the Shandong Peninsula has developed since 7 kyr B.P (Li et al., 2014; Yang and Liu, 2007), and the sediment supply from the Yellow River has varied substantially over that time. These model results are limited to a one-year simulation and any inferences about longer-term accumulation introduce increasing uncertainty. However, some of the key seasonal variation in transport processes may be generally relevant at longer-time scales than the simulation period, and may relate to longer-term accumulation patterns.

4. Model evaluation

To evaluate the tides, the model is first run with only tidal forcing. The modeled sea-surface elevation results are used to calculate the harmonic constants of the M_2, S_2, K_1 and O_1 constituents, which are the dominant semidiurnal and diurnal constituents in the Bohai Sea, the Yellow Sea and the East China Sea. The modeled tide amplitudes and phases of M_2, S_2 and O_1 constitutes match well with the previously published works (Editorial Board for Marine Atlas, 1992) and differences are < 5%. The modeled K_1 tide amplitude seems to be ∼10% greater than observed (not shown here), perhaps due to the use of a uniform bottom toughness height ($z_0 = 1.0 \times 10^{-5}$ m) or errors at the open boundary.

In addition to the basin-scale maps of tidal amplitude and phase, water level, vertically averaged current speed, and current direction from the model are compared with observed time-series data from coastal regions of the eastern Yellow and Bohai Seas (stations C1 and C2 in Fig. 1, data from Qiao et al. (2016)). Model results were evaluated with the coefficient of determination (R^2), the root-mean-square error (RMSE), and the skill score (SS; Murphy, 1988; Ralston et al., 2010; Luo

Table 2
Evaluation of model performance.

Parameter	R^2	Skill Score	RMSE	Best-fit slope
Significant wave height (Nov.)	0.64	0.60	0.34	0.90
Water_level (Jun.)	0.88	0.84	0.12	0.84
Current_speed (Jun.)	0.64	0.39	0.08	0.62
Water_level (Sep.)	0.98	0.92	0.16	1.01
Current_speed (Sep.)	0.57	0.54	0.07	0.93
Temperature (May and Nov.)	0.75	0.60	2.32	1.20

et al., 2017) (see Table 2).

Comparisons between numerical results and observational data in June and September 2012 indicate that model results generally agree with the observations at these locations (Fig. 2; Table 2). Quantitative skill assessments give R^2 and SS of ∼0.9 for water level, and somewhat lower values for current speed ($R^2 = 0.6$, SS = 0.4–0.6). Based on the comparison between model results and available observations, the model appears to be reasonably reproducing the regional tidal currents. Similarly, the input wind data from the ECMWF model corresponds well with observed winds at station C2 in November 2012 (Fig. 2). The wave model was run using default input parameters, and the significant wave heights during this period agree with the observational data ($R^2 = 0.64$) (Table 2).

The model is also compared with observations of temperature and SSC during cruises of R/V DONGFANGHONG 2 in the Bohai and Yellow Seas in May 2012 (18 days) and November 2012 (19 days) (Wang et al., 2014b) (Fig. 3). The simulated temperature fields generally match the observations well ($R^2 = 0.75$, SS = 0.6). The simulated temperature is slightly lower than the observations (Fig. 3 (I)), perhaps due to uncertainty in the input heat flux from ECMWF or the use of a uniform irradiance attenuation rate.

In addition to the basic absorption by the seawater, transmission of solar irradiance in the Yellow Sea depends on suspended sediment concentration (Lin et al., 2009). When the vertical mixing is strong, the vertical distribution of irradiance has little effect on the vertical distribution of water temperature. However, when the stratification becomes strong, the vertical distribution of the heat input by solar irradiance greatly impacts the temperature profile. The model was run using different Jerlov water types, which classify the spectral optical attenuation depth for different water bodies (Jerlov, 1968). Using Jerlov water type I, which represents water clarity in the open ocean, leads to concentrated heating near the seabed, strong convective vertical mixing near the coast and large values of bottom temperature seaward. Jerlov water types II and III are typically used in coastal regions, with different values for the irradiation absorbed in the upper 5 m (R) and attenuation length scales in the upper 5 m (ζ_1) and over 10–40 m (ζ_2). With larger R and smaller ζ_1 and ζ_2, more irradiation is absorbed in the upper 5 m and the attenuation depth decreases. In observations from March 2005, the vertical distribution of the average irradiance in Yellow Sea (Lin et al., 2009) is consistent with the distribution of Jerlov water type III. However, in summer, the SSC is less than that in March, which decreases the attenuation rate. Using Jerlov water type III (R = 0.78; $\zeta_1 = 1.4$; $\zeta_2 = 7.9$), the thermal front seaward of the Shandong Peninsula in July was shifted farther onto the shelf compared with the frontal position using Jerlov water type II (R = 0.77; $\zeta_1 = 1.5$; $\zeta_2 = 14$). Importantly, the bottom temperature was much lower using Jerlov water type III than using Jerlov water type II. The bottom temperature and the position of the thermal front using Jerlov water type II were more consistent with observations, so it was used in the simulations presented here.

For suspended sediment, both observations and the model show that concentrations in May are generally less than in November, and the greatest concentrations are located in the coastal region around the Chengshantou Cape (the east tip of the Shandong Peninsula, see Fig. 1 (a)). The modeled concentrations in May are larger, about twice that of
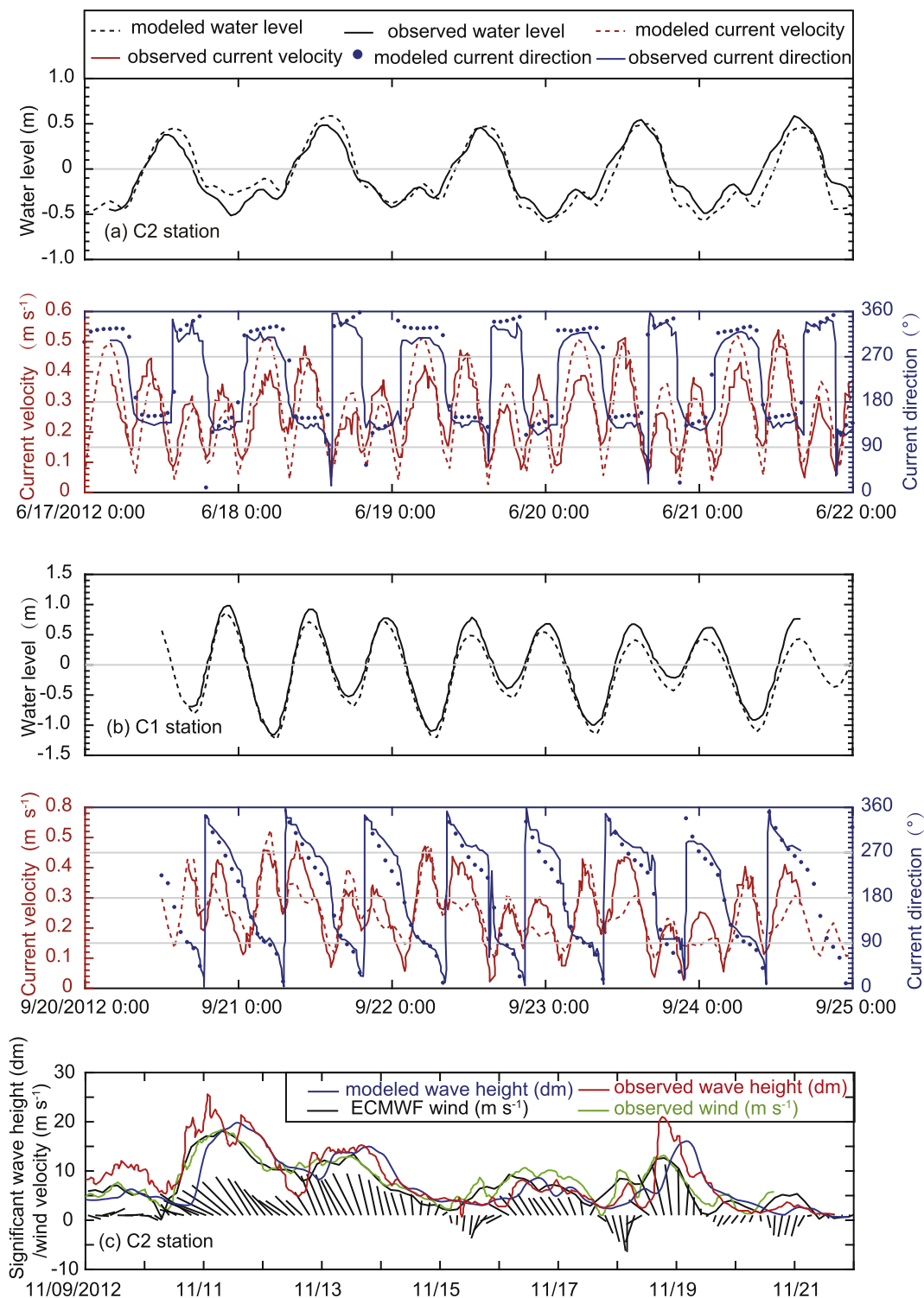
Fig. 2. Comparison of measured data and modeled data (water level, depth averaged current speed and current direction) at Station C2 in June (a) and at Station C1 in September (b). (c) Comparison between measured data and model results at Station C2, including wind speed and significant wave height, black arrows represent wind direction. The observed data are from Qiao et al. (2016).

mean observations (Fig. 3b), especially near the bottom where SSC is only ∼ 10 mg L^{-1}. The modeled vertical gradient in SSC is greater than the observations (Fig. 3 (a), (c) and (b), (d)), perhaps due to uncertainties or temporal variations in sediment settling velocity and surface erosion rate. In November, the model results agree well with the observations (R^2 = 0.53), and there is strong correspondence in the spatial distribution of SSC, in particular near the Chengshantou Cape (Fig. 3 (e), (f), (g), (h)). These model evaluations are limited by the

availability of observational data, but the model generally captures the spatial and seasonal variations in SSC, and of tidal-to-event-scale variation of currents and waves, which provides a basis for investigating the sediment-transport and deposition processes.
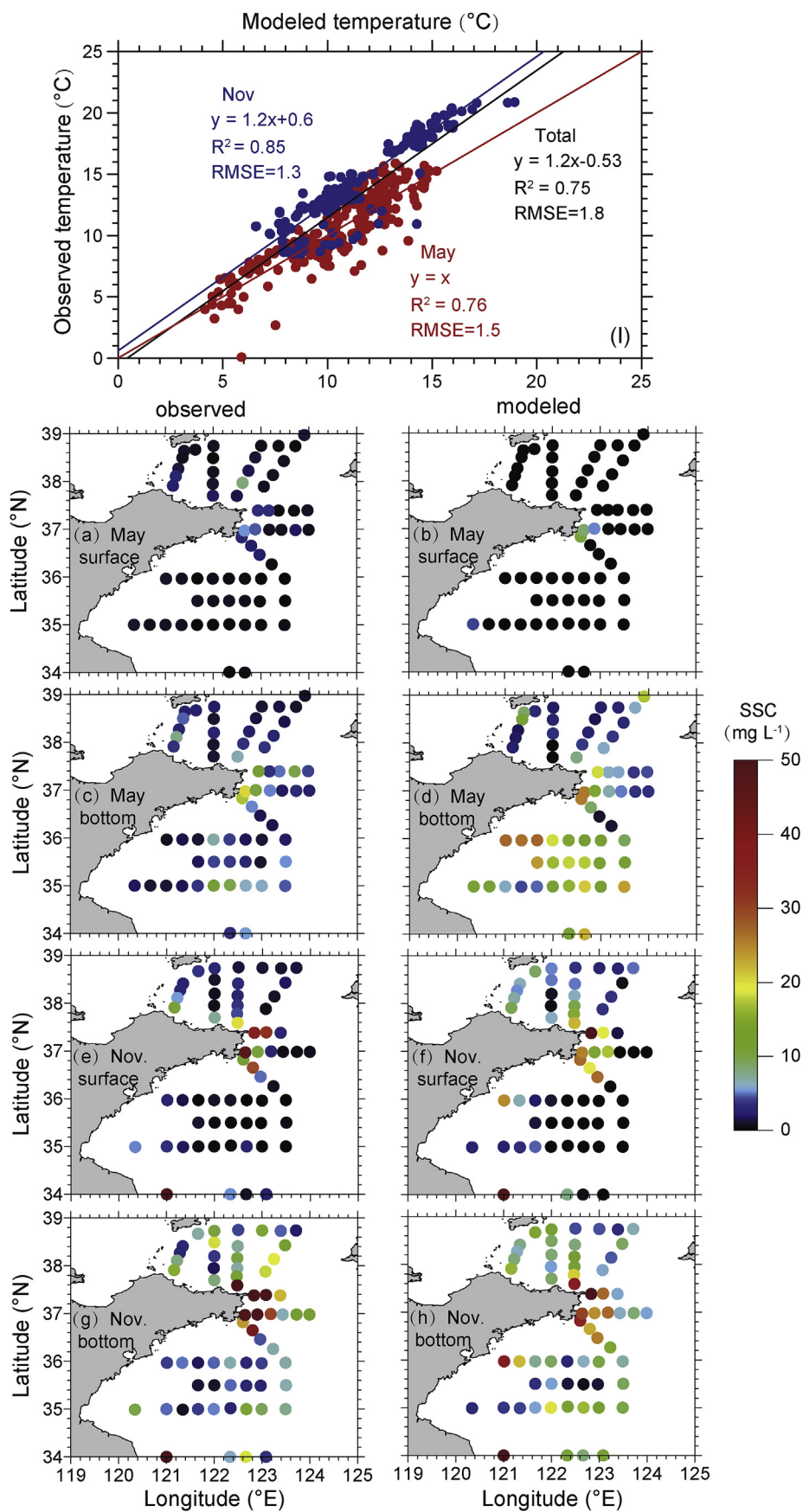
Fig. 3. (Upper) Comparison of temperature between observations and modeled results in May and November. (lower) Comparison of suspended-sediment concentration between observations (surface: (a), (e); bottom: (c), (g)) and modeled results (surface: (b), (f); bottom (d), (h)) in May, 2012 and Nov, 2012. The bottom SSC was measured at 2–3 m above the seabed, the surface SSC was measured at 2–3 m under the sea surface.
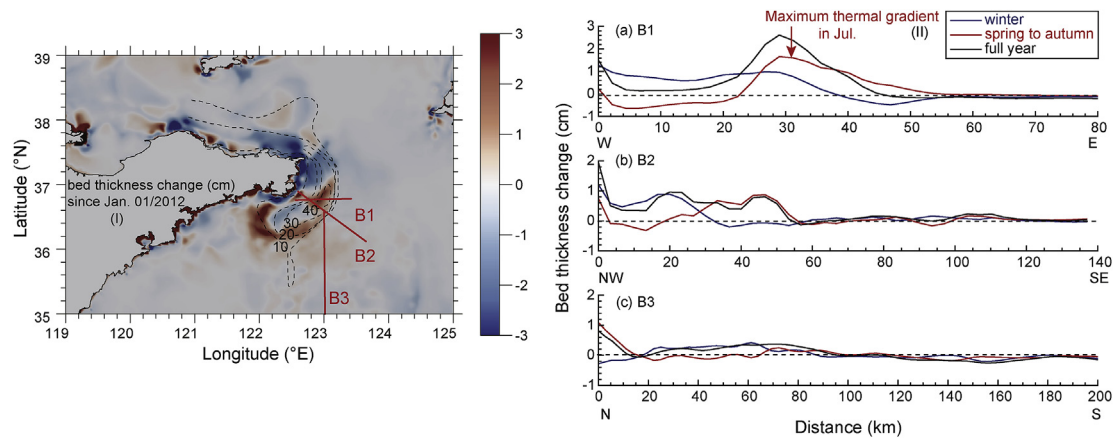
Fig. 4. (left) Bed-thickness change from 1 Jan. 2012 to 1 Jan., 2013. The black dashed lines indicate the isopach map (m) of the mud clinoform from Yang and Liu (2007); (right) Bed-thickness change along model transects for a full year and separating the spring to autumn (April to November) and winter (December to March) periods for transects B1 (a), transect B2 (b), and transect B3 (c).

5. Results

5.1. Sediment accumulation on the clinoform

Based on the sub-bottom profiles acquired from geophysical observations, Yang and Liu (2007) documented a distinct omega-shaped muddy clinoform in the Yellow Sea, defined by its maximum accumulation rate being located offshore rather than a classic sigmoidal-shaped clinofom with monotonic seaward decreasing accumulation rate. Our modeling results produce a region of focused net sediment deposition at the annual time scale (Fig. 4) that presents a similar form as the cross-shelf structure of clinoform in observations (Yang and Liu, 2007). The region of sediment deposition over the full-year model simulation extends southward from the east tip of the Shandong Peninsula, and gradually thins, widens, and diminishes into the central south Yellow Sea. The modeled depo-center corresponds to the location of the thermal front that will be discussed subsequently.

Three transects of seabed deposition thickness are extracted from the model results at the same locations as the seismic sub-bottom profiles of Yang and Liu (2007), and the model results show depositional patterns similar to the stratigraphic sequences inferred from the observations with high deposition rates offshore and decreasing bidirectionally. Considering the deposition after a full year of simulation at transects B1 and B2, a nearly symmetric offshore mud mound is found in the model, which is similar to the seismic profile of the omega-shaped clinoform (Yang and Liu, 2007). Based on previously published documents and samples collected in 2004–2010, Qiao et al. (2017) estimated that the modern sediment accumulation rate around the Shandong Peninsula varied from 0 to 0.96 cm yr^{-1} with an average rate of 0.37 cm yr^{-1}. The modeled sediment deposition rates are greater by > 2 than the estimates from observations (model results: 0–2.5 cm yr^{-1}), perhaps because the model does not include bed consolidation. Greater deposition rates are also consistent with the modeled greater SSC in the summer than in observations. At transect B3, farther away from the sediment deposition center, similarly high sediment deposition rates are only found in the northern part of the transect, near the intersection of transects B2 and B3, which is consistent with the sediment accumulation patterns from the seismic transects.

While sediment accumulation patterns over the full-year model simulation reflect the longer-term accumulation associated with the omega-shaped clinoform, significant seasonal differences in sediment deposition and erosion patterns are also identified from the model simulation (Fig. 4 right panel and Fig. 5). The net sediment deposition during the spring-to-autumn period presents a local offshore maximum near the full-year depo-center, whereas landward on the shelf the seabed is eroded during this period. Such erosion (Fig. 5c) occurs

mainly in August during passage of a strong typhoon (Typhoon Bolaven, August 20–29, 2012) that greatly increased the wave height and bottom shear stress in this region. From April to July, the center of sediment deposition is located offshore. The moderate resuspension of sediment on the shelf during this period due to weak wind forcing and enhanced stratification that limit the sediment supply and reduce the deposition rates compared to other periods. In the fall as the coastal water cools and wind speed increases, vertical mixing becomes stronger and SSC increases in the coastal area, resulting in greater net deposition rates than those during April–July, and shifting the depo-center farther seaward. In contrast, sediment deposition is greater near the coast and decreases seaward in winter (Fig. 4 right panel and Fig. 5). We subsequently use the model along with observations to examine seasonal differences in the hydrography and sediment transport that lead to these seasonal sedimentary patterns.

5.2. Seasonal variation of clinoform development

5.2.1. Seasonal variation of temperature and suspended sediment from observations

Data from cruises in different years are used to illustrate the strong seasonal variability in hydrography and suspended sediment near the Shandong Peninsula, recognizing that inter-annual variability also plays a role in the longer-term sediment accumulation patterns. The observational datasets of temperature and SSC were obtained from cruises *R/V* DONGFANGHONG 2 in the Bohai and Yellow Seas from multiple years to span the seasonal variation: May 2012 (18 days), November 2012 (19 days), January 2016 (17 days), and July 2016 (21 days). Water samplings were operated at 3 or 4 specific layers depending on the local water depth. The bottom water samples were taken at 2–3 m above the seabed. Details of water sampling and data collection can be found in Wang et al. (2014b). The seasonal variation in the horizontal and vertical structures of SSC and temperature are shown in Fig. 6 and Fig. 7, respectively.

In May 2012 (early summer), the water column was weakly stratified and a bottom thermal front had formed with warmer waters on the shelf. During this period, the bottom SSC was ~ 20 mg L^{-1} on the shelf east of the Shandong Peninsula, and it was < 10 mg L^{-1} elsewhere (Figs. 6 (a) and Fig. 7 (a)). The shallow regions and near-surface layer were significantly warmer due to the increasing solar radiation from spring to summer, as in the observations from July 2016 (summer). The temperature of the offshore deep water (about 8 °C) was almost unchanged as compared with the observations in May 2012. Consequently, the water column was highly stratified with an intensified cross-shelf thermal gradient in the summer. The SSC was greater in July 2016 than in May 2012, with bottom SSC > 30 mg L^{-1} east of the
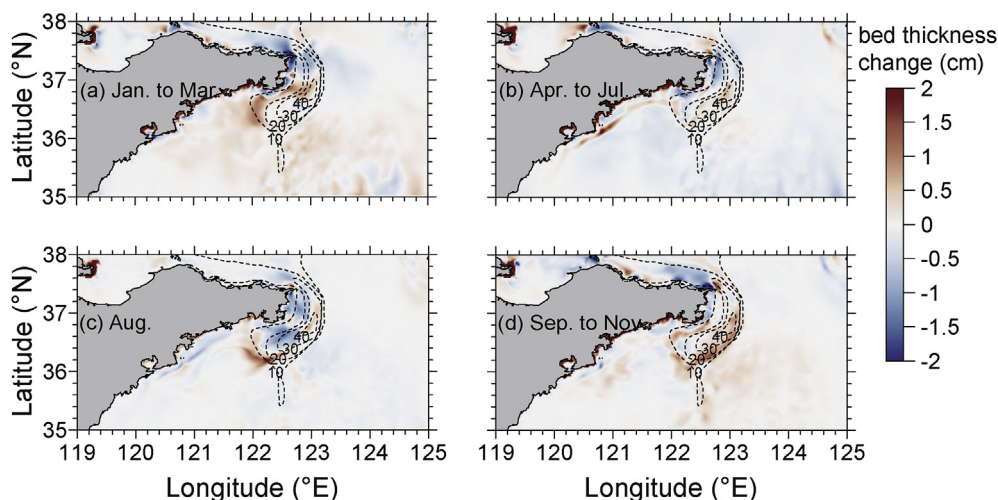
Fig. 5. Bed-thickness change for January to March (a), April to July (b), August (c) and September to November (d). The black dashed lines indicate the isopach map (m) of the mud clinoform from Yang and Liu (2007).

Shandong Peninsula, and SSC decreased seaward from the shelf as in the spring (Figs. 6 (b) and Fig. 7 (b)).

In November 2012 (transition from autumn to winter), the upper layer and shallow coastal water had cooled, while the temperature of the offshore deep water increased compared to the summer conditions. The thermocline moved downward and the bottom thermal front moved seaward. The SSC east of the Shandong Peninsula increased to ~80 mg L^{-1} and decreased seaward gradually (Figs. 6 (c) and Fig. 7 (g)). In January 2016 (winter), the water column was well mixed with vertically uniform temperature profiles. The bottom temperature distribution was opposite to that in summer, with colder water near the coast and warmer water in the central Yellow Sea. The SSC was greatest during the winter observations, with nearly uniform vertical distribution (Figs. 6 (d) and Fig. 7 (h)).

5.2.2. Seasonal variation of sediment transport and deposition from model results

The observed seasonal patterns of water temperature and SSC were

satisfactorily reproduced by the model, and the model results are used to illustrate the strong seasonal variability of sediment transport and deposition. We analyzed the model outputs in two representative months: July for summer conditions and December for winter. According to Wright and Nittrouer (1995), the fate of sediment dispersed from the river into the coastal ocean involves at least four stages: supply via plumes, initial deposition, re-suspension and transport by marine processes, and long-term net accumulation. About 90% of the sediment from the Yellow River is discharged to the Bohai Sea from mid-June to mid-August (Wang et al., 2014b). Almost 70% of that sediment deposits on the delta within 15 km of the river mouth (Qin and Li, 1983; Bi et al., 2010) due to the weak hydrodynamic forcing and strong stratification in that region in summer. Resuspended sediment escapes from the Yellow River Delta to the Yellow Sea mostly during winter (Bi et al., 2011; Wang et al., 2016), but this represents only 1%~15% of the Yellow River sediment discharge (Qin and Li, 1983; Alexander et al., 1991; Martin et al., 1993; Jiang et al., 2000; Li et al., 2010; Bi et al., 2011; Wang et al., 2016). Due to the combined effects of
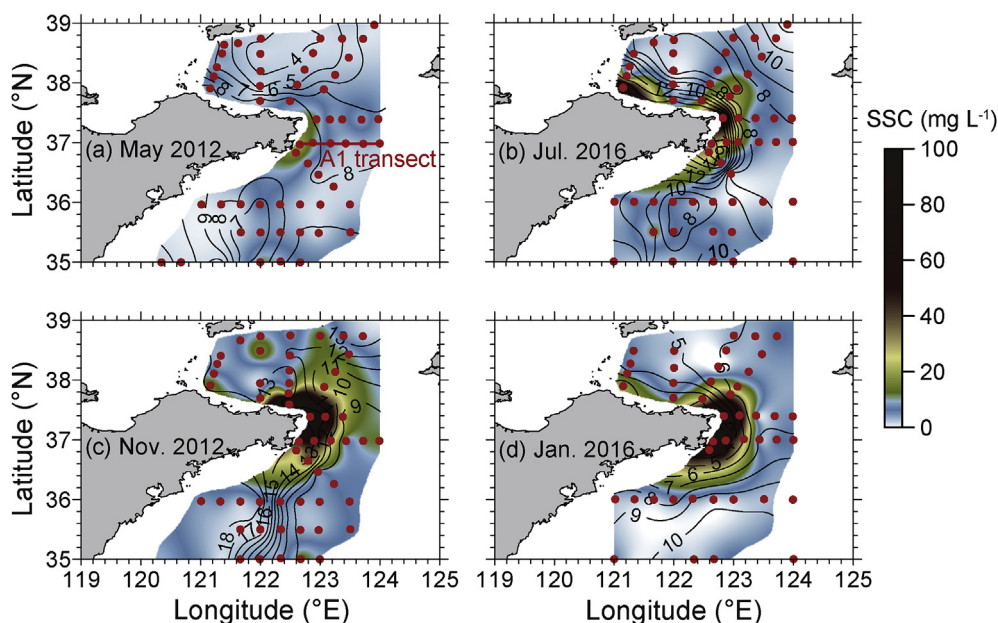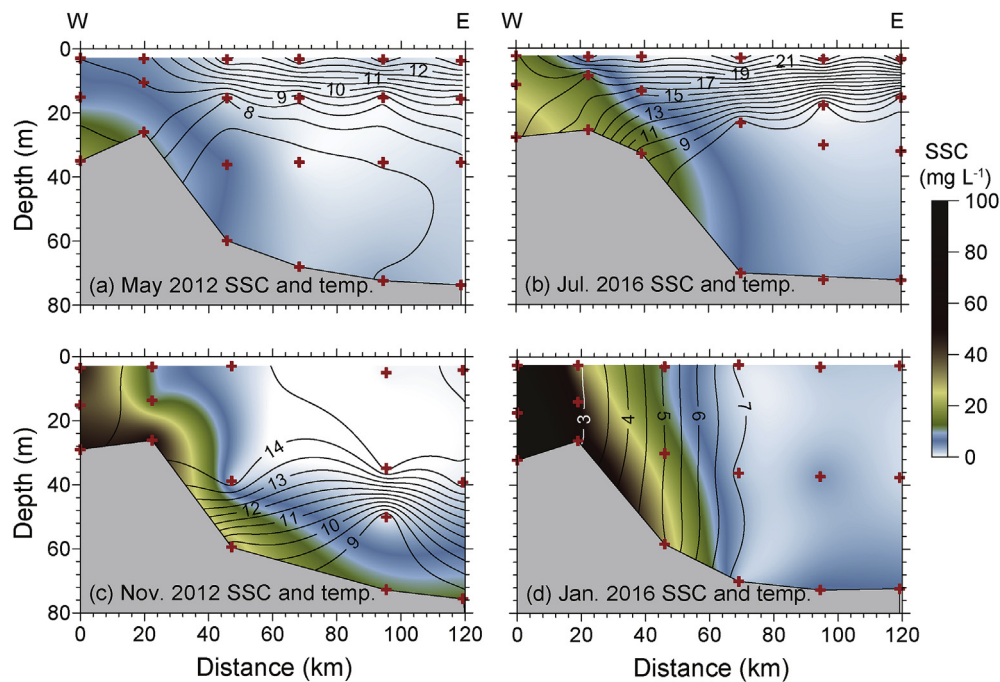

Fig. 6. The bottom horizontal distribution of observed SSC (color shading, mg L^{-1}) and temperature (contour, °C) in four seasons. The dots denote the observation sites. (For interpretation of the references to color in this figure legend, the reader is referred to the Web version of this article.)

Fig. 7. Vertical distribution (A1 transect in Fig. 6) of observed SSC (color shading, mg L^{-1}) and temperature (contour, °C) in four seasons. The symbols of cross denote the locations of observation and water sampling. (For interpretation of the references to color in this figure legend, the reader is referred to the Web version of this article.)

climate change and human activities in the watershed of Yellow River, the sediment supply decreased sharply from a widely cited sediment load of 1.08 Gt yr^{-1} to 0.14 Gt yr^{-1} in 2013 (Wang et al., 2017). In the simulation year of 2012, the sediment supply was only 180 million metric tons.

The clinoform region off the Shandong Peninsula is located ~350 km away from the present Yellow River mouth, therefore sediment transport from the delta to the clinoform region is indirect that requires wave-supported resuspension and transport by longshore currents. With this model of a particular year it is hard to directly address how trends in sediment supply at time scales of decades to centuries or its inherent inter-annual variability may affect transport rates from the delta to the clinoform region. However, the basic transport mechanisms and seasonal variation identified from the simulation are expected to be generally relevant to this region, albeit with the potential for modulation in amplitude due to changes in sediment supply.

In July (summer), southerly winds prevail and are typically weak, but they contribute to the residual currents and sediment transport near the coast. In the middle of the Yellow Sea a cyclonic geostrophic current develops mainly due to the pressure gradient and the Yellow Sea Cold Water Mass produced by winter cooling (Zhao, 1987; Naimie et al., 2001) (Fig. 8 (a)). Sediment is transported eastward and then southward by the cyclonic geostrophic current. Based on model experiments without wind forcing, the coastal current would continue southward along-shelf south of the Shandong Peninsula in the absence of summer winds. However, with realistic southerly summer winds the modeled coastal current is reversed and flows northeastward weakly in this region (Fig. 8 (a)). This convergent wind-driven flow in the model is consistent with observations using drifters (Pang et al., 2004).

The stratification and the near-bottom cross-shelf thermal gradient is strong during this time (Fig. 9 (a) and (b)). Both greater SSC and longshore sediment transport are found at the landward side of thermal front (Fig. 9 (a) and (b)). Near the coast, stronger waves and currents induce greater bottom shear stress (Fig. 10 (a)) and greater SSC, and sediments are transported primarily along the coast by the cyclonic current. Stratification suppresses turbulence in the upper water column, limiting the vertical extent of sediment mixing to a thin bottom

boundary layer (Fig. 11 (a)). The stronger stratification within the thermal front and the offshore area consequently reduces turbulence within the bottom boundary layer (or eddy viscosity from the model results) and bed shear stress, leading to large spatial gradients in SSC between the onshore and offshore regions (Figs. 8 (a) and Fig. 9 (a) and (b)).

The spatial differences in stratification, resuspension, and vertical mixing produces a convergence in sediment transport, with greater deposition rates around the thermal front (Geyer, 1993). Sediment is transported to the thermal front area by the coastal current and the basin-scale cyclonic current, the thermal front acts as a barrier that constrains the seaward transport of sediment. Due to the weak winds and waves in the spring and summer, SSC on the shelf becomes less than ever as the thermal front starts to develop, which in combination leads to lower deposition rates. However, as stratification weakens and bed shear stress increases in the coastal region from September to November due to the enhanced wave action and sea surface cooling, the SSC increases significantly, increasing the sediment availability and deposition rates at the front. Consequently, the maximum deposition rates occur during the fall, when the thermal front still exists but the supply of sediment has increased due to more active sediment resuspension (Fig. 5 (b) and (d)).

In December, strong northerly winds dominate over the Yellow Sea, affecting the wave height, residual circulation, thermal structure and the corresponding sediment transport and deposition patterns. The basin-scale cyclonic current during the summer has been replaced by two counter-rotating gyres (Fig. 8 (c)). Stronger northerly winds intensify both the southward Yellow Sea Coastal Current and the compensating northward Yellow Sea Warm Current, producing lateral shear between the two current systems. Increased wave actions together with enhanced currents induce intense bottom shear stress (Fig. 10 (b)) and strong vertical mixing (Fig. 11b), which lead to greater SSC (Fig. 8 (c)) and southward sediment transport along the coast, whereas seaward of the shear zone, the northward transport by the Yellow Sea Warm Current becomes weaker (Fig. 8 (d)).

In winter, the water column becomes well mixed and the weak cross-shelf temperature gradient (Fig. 9 (c) and (d)) has little effect on
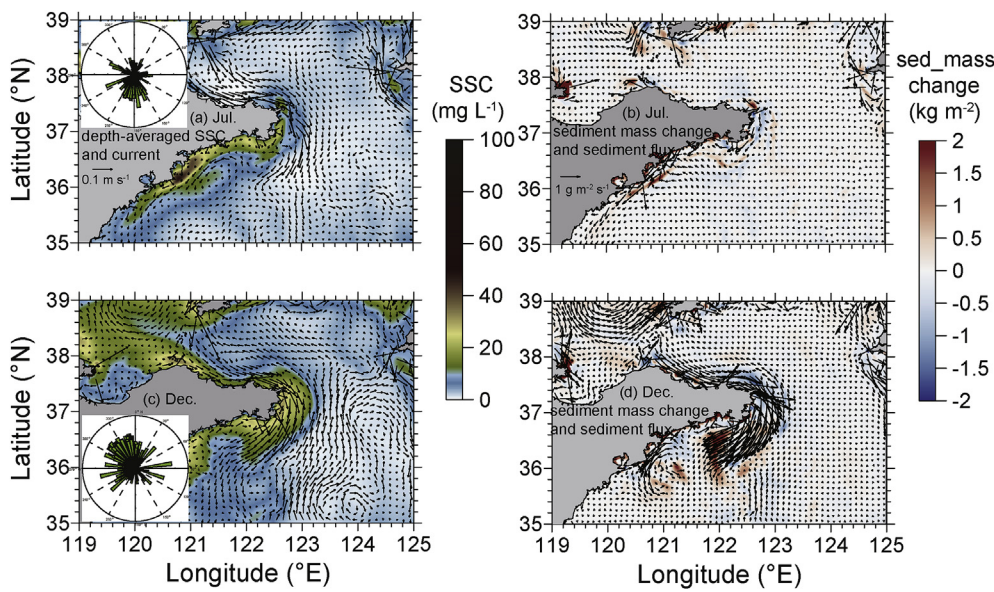
Fig. 8. Horizontal distribution of depth-averaged SSC (color shading, (a), (c)), current (arrow, (a) (c)), wind rose diagram ((a), (c)), bed-sediment mass change during one month (color shading, (b), (d)), and depth-averaged sediment transport (arrow, (b), (d)) in July and December. (For interpretation of the references to color in this figure legend, the reader is referred to the Web version of this article.)

sediment trapping and deposition. Both SSC and sediment transport are the greatest in the coastal area due to energetic wave actions and currents, and decrease seaward gradually (Fig. 9 (c) and (d)). Without the focused trapping at the thermal front, the deposition rate is greater onshore and decreases seaward, evidently in contrast to the summer when the greatest deposition rates occur around the thermal front. To the southwest of the Shandong Peninsula the coastal current expands and decelerates as the shelf widens, and this reduction in velocity results in decreased sediment flux and increased sediment deposition broadly to the south of the Shandong Peninsula. This depositional region gradually thins and widens along the shelf and into the central south Yellow Sea (Fig. 8 (d)).

The model results demonstrate that sediment deposition patterns in the Yellow Sea vary seasonally (Figs. 4 (b), Fig. 5) depending on the stratification and horizontal temperature gradients. The net accumulation over the annual cycle primarily results from the deposition at the thermal front during spring to autumn, and it is greatest in the region of the omega-shaped clinoform. The maximum deposition rates occur during the seasonal transition from September to November, when the

thermal front that develops in summer still exists and the sediment in the water column increases landward of the front due to stronger winds, waves and sea-surface cooling. In contrast, the greatest SSC and sediment transport rates occur in the winter when the stratification disappears and the thermal front weakens so it has little effect on the sediment trapping.

6. Discussion

These model results together with previous studies (Zang et al., 2017; Wang et al., 2013) demonstrate that thermal front plays a critical role in trapping the fine-grained suspended sediment near the clinoform. Li et al. (2016) found the Yellow Sea Cold Water Mass grew in summer and declined in autumn based on in-situ observations, corresponding seasonal shifts in the location of the thermal front. Based on a stratification parameter, Pan (1993) found that from May to August the thermal front shifts landward and intensifies as the surface heat flux to the ocean increases, and then moves seaward from September to November when the seawater is cooling. Zhao (1987) proposed that the
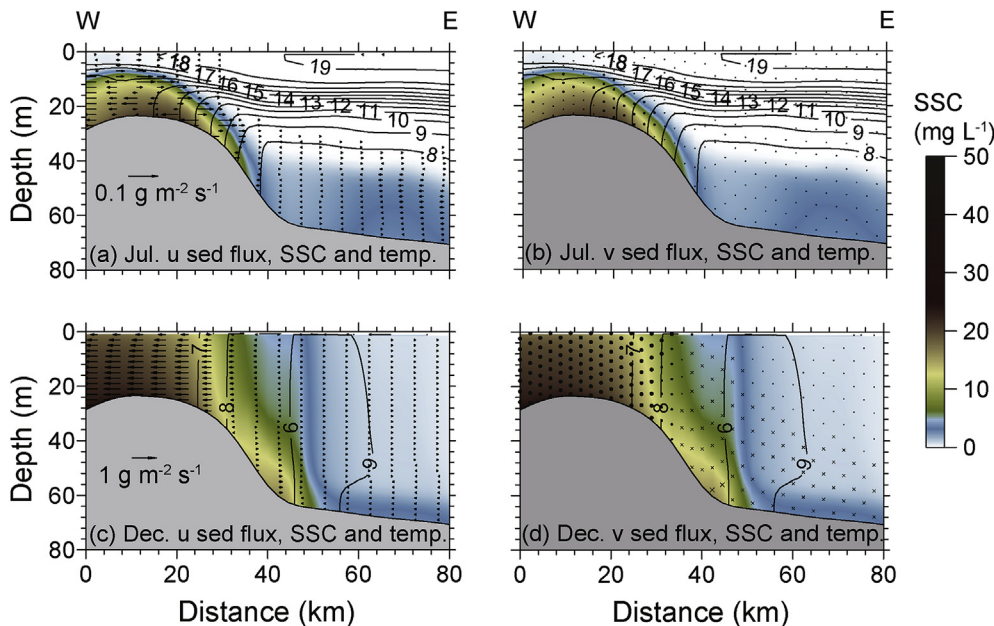

Fig. 9. Vertical distribution of suspended sediment concentration (color shading), sediment flux (arrow), and temperature (contour) in transect B1 (shown in Figs. 1 and 4) during July and December (a, b, c, d) for model. (For interpretation of the references to color in this figure legend, the reader is referred to the Web version of this article.)
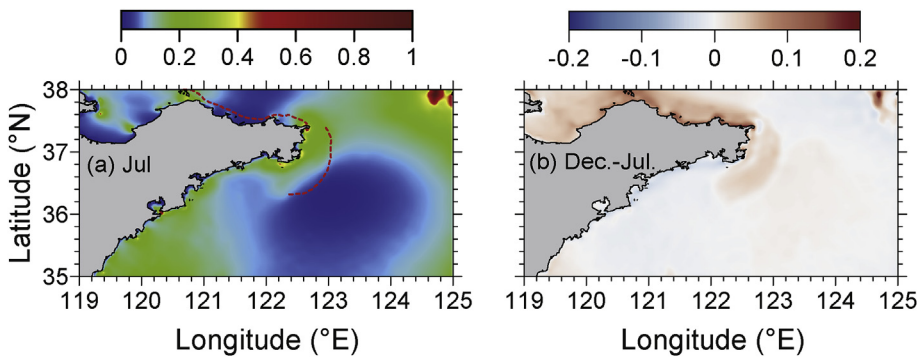
Fig. 10. (a) Horizontal distribution of maximum bottom shear stress in July (N m^{-2}, red dashed line represents the location of thermal front). (b) difference of maximum bottom shear stress between December and July (N m^{-2}). (For interpretation of the references to color in this figure legend, the reader is referred to the Web version of this article.)

Fig. 11. Monthly averaged vertical distribution of eddy viscosity (color shading, m^2 s^{-1}) and monthly averaged temperature (contour, °C) in transect B1 in July (a) and December (b). (For interpretation of the references to color in this figure legend, the reader is referred to the Web version of this article.)

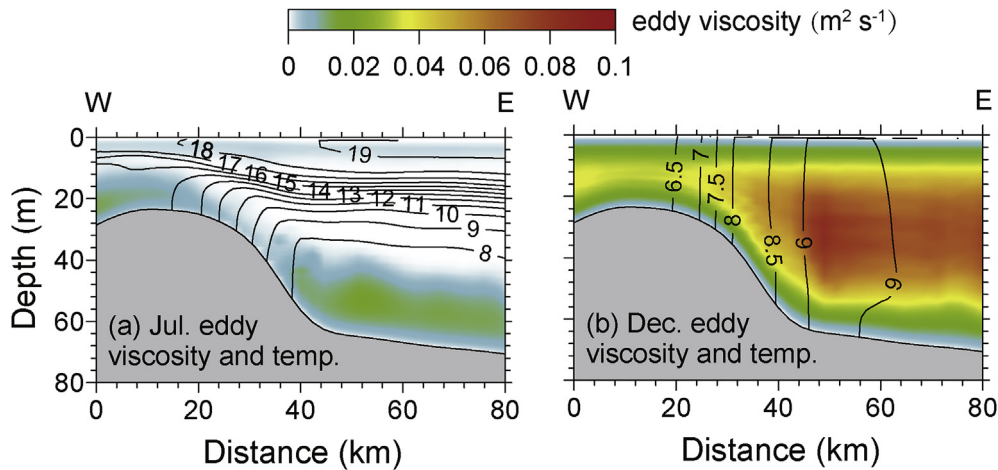geostrophic coastal current seaward of the Shandong Peninsula moves farther seaward from summer to autumn, as a result of the recession of the Yellow Sea Cold Water Mass.

Following Wang and Liu (2009), the location of the thermal front is determined based on the horizontal temperature gradient (G).

$$G = \sqrt{(\partial T/\partial x)^2 + (\partial T/\partial y)^2}$$

where T is the water temperature (unit: °C). The location of the thermal front is defined by the location of the maximum temperature gradient. From July to November, the position of the thermal front shifts seaward into deeper water (Fig. 12 left panel). Correspondingly, the region with greater SSC area and sediment deposition also moves seaward seasonally (Fig. 12 right panel and Fig. 13). This seasonal shift in the location of front and region of maximum deposition corresponds with the region of the broad topset for the clinoform (Fig. 13).

According to Simpson and Hunter (1974) and Zhao (1985), the formation of a tidal mixing front in stratified shelf waters depends on the balance between the increase in potential energy due to surface heat flux and turbulent mixing due to tidal currents, which can be represented by:

$$\frac{H}{u^3} = \frac{8c\rho k\varepsilon}{3\pi\alpha g Q}$$

where u is the surface tidal velocity amplitude, c is the specific heat, ρ is the water density, k is the drag coefficient, ε is a mixing efficiency, α is the thermal expansion coefficient, and Q is the surface heat flux. H represents the water depth at which stratifying and destratifying processes balance. At the water depth greater than H, turbulent energy cannot fully mix away the stratification created by the heat flux, and in water depth less than H the tidal mixing is expected to homogenize the water column.

Since tidal currents do not vary over seasonal cycle, the location of the thermal front may change corresponding to the seasonally varying surface heat flux that is associated with the sea and air temperature and the solar radiation. When Q decreases seasonally, the corresponding H becomes larger and the thermal front location moves seaward, and vice versa. At shorter time scales, the thermal front is expected to move seaward during spring tides and move landward to shallower water during neap tides (Simpson and Bowers, 1981; Mountain and Taylor, 1996).

In contrast to the well-mixed conditions in the Irish Sea described by Simpson and Hunter (1974), weak stratification remains in the upper water column landward of the bottom thermal front in the Yellow Sea from July to September (Fig. 12, right panel). The complete mixing in Irish Sea case leads to both surface and bottom fronts, whereas only a strong bottom front forms around the Shandong Peninsula. A cross-front gradient in stratification is created in both cases, which results in cross-front gradients in sediment resuspension and deposition by tidal currents.

The critical value for the Simpson-Hunter number (H/u^3) changes seasonally with the net heat flux (Q), affecting the cross-shelf location of the thermal front. From July to November the surface heat flux decreases and the position of the thermal front shifts seaward into deeper water (Figs. 14 and 12). The position of the thermal front also shifts fortnightly due to changes in the tidal current, consistent with the Simpson-Hunter framework (Fig. 14). During spring tides, tidal mixing in the coastal region increases and the position of the thermal front shifts seaward to deeper water. During neap tides, tidal velocities decrease and the front moves landward to shallower water. The position and intensity of the thermal front may also vary inter-annually with variation in sea surface heat flux. For example, in most EI Nino years, the depth of the stratification decreases and the position of the thermal
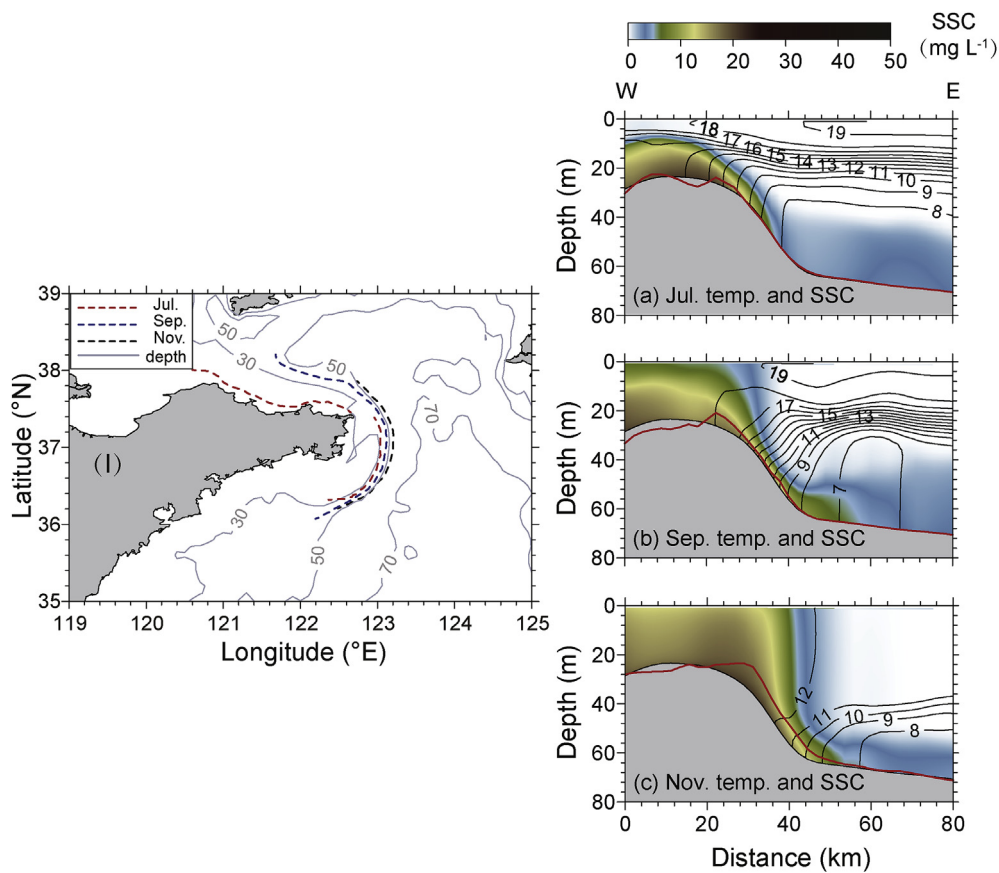
Fig. 12. (left) The thermal front locations in July, September and November (dashed line) and bathymetry (grey contour). (right) The vertical distribution of suspended sediment concentration (color shading, kg m^{-3}), temperature (contour, °C) and 2000 times of bed thickness change (red solid line) in July (a), September (b) and November (c). (For interpretation of the references to color in this figure legend, the reader is referred to the Web version of this article.)

front shifts seaward (Bai et al., 2004).

The high deposition rates focused offshore depend both on the thermal front to create a region of enhanced sediment trapping and a sufficient sediment supply. As noted above, the Yellow River-delivered sediment primarily accumulates within the subaqueous delta and only a limited amount of fine-grained sediment is exported to the Yellow Sea (Bi et al., 2011; Wang et al., 2016), so sediment transport near the clinoform depends primarily on local redistribution in summer. The fluvial sediment supply in the simulation year of 2012 was only 0.18 Gt, representing just 16% of the estimated mean sediment load of 1.08 Gt yr^{-1} (Wang et al., 2007). East and south of the Shandong Peninsula, strong tidal currents and an erodible bed put sediment in the water column that supplies the enhanced deposition around the thermal front from spring to autumn. In contrast, north of the Shandong Peninsula, the tidal currents and wave energy are weaker and sediment resuspension is less, so sediment deposition rates are small despite the

presence of a thermal front there near the coastline in July. The shelf is broader north of the Shandong Peninsula, so the tidal mixing front shifts far seaward late in the summer (Fig. 12 (I), left panel). Resuspension and vertical mixing increase SSC near the coast due to enhanced wave actions and weakened stratification, resulting in net erosion in this region (Fig. 5). The thermal front to the north of the Shandong Peninsula is far from the region of sediment resuspension, so deposition rates around it remain relatively small. Observations from north of the Shandong Peninsula have noted a sigmoidal-clinoform (Liu et al., 2004) with sediment deposition decreasing seaward, in contrast to the high sediment deposition in a focused region offshore.

Sediment off the Shandong Peninsula originated from the Yellow River, and over the last 2000 years large-scale channel migrations of the lower Yellow River have occurred more than 20 times and the location of river mouth has moved five times (Xue, 1993). Under the influence of intensive human activities, the sediment load of Yellow River has
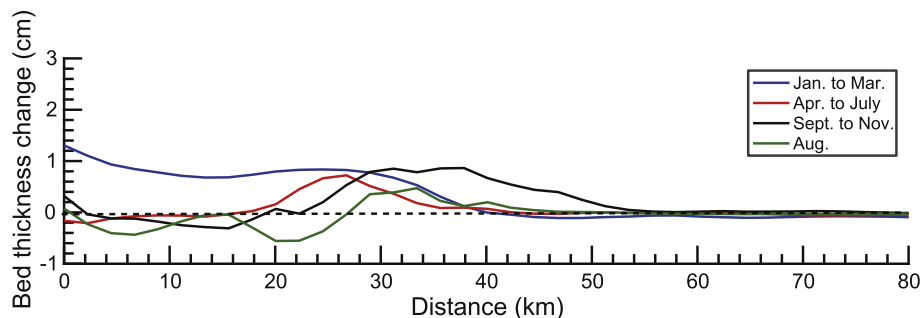
Fig. 13. Bed-thickness change for January to March, April to July, September to November, and August in transect B1 (shown in Fig. 1).
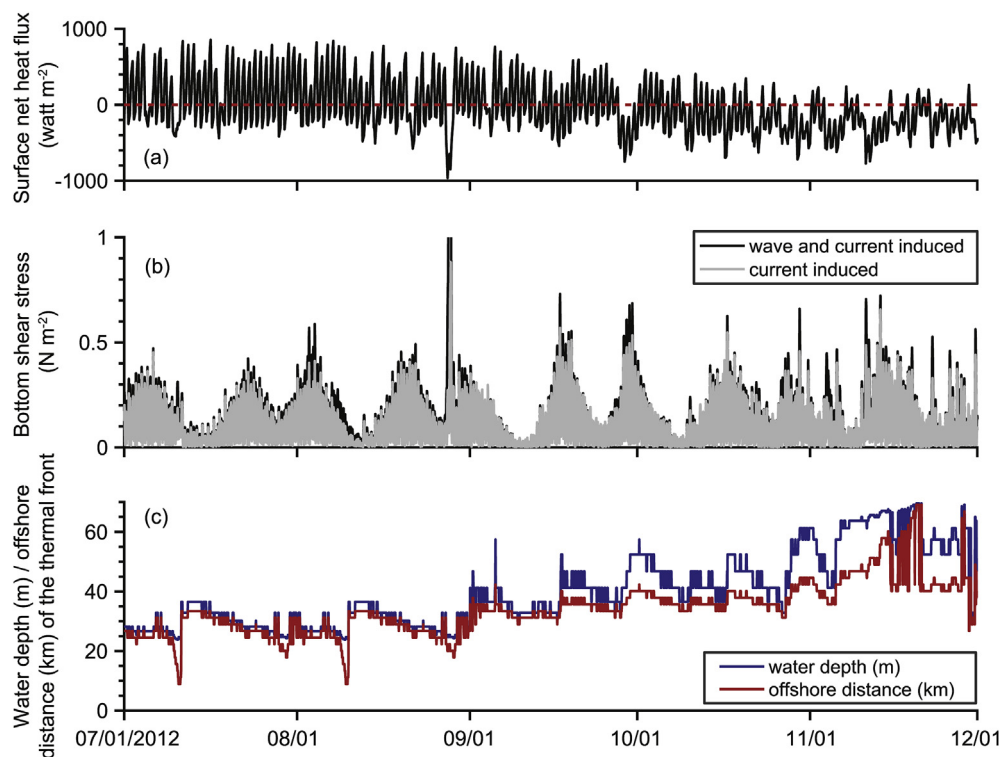
Fig. 14. Time series of (a) average sea-surface net heat flux (watt m^{-2}), (b) current-induced and wave-current-induced bottom shear stress (N m^{-2}) (c) water depth and seaward distance of the thermal front in transect B1.

experienced stepwise decreases due to reservoir retention (Wang et al., 2007). As the major contributor of the sediment to the study area, the frequent channel migrations and decreased sediment discharge of the Yellow River also are significant factors contributing to the longer-term variability in regional sediment-transport process.

Based on the one-year of model results representing the modern circulation and sediment transport, we could only address net sediment deposition over that period, and are drawing inferences about the relation between the deposition in the model results and accumulation at longer-time scale. In the model, the seabed east of the Shandong Peninsula is accretionary over the whole year, suggesting a trend that may relate to the longer-term accumulation. Over the past 7000 years during which the clinoform formed (Li et al., 2014; Yang and Liu, 2007), the circulation patterns and marine sedimentary environment have been relatively stable (Zong, 2004; Liu et al., 2010; Li et al., 2010, 2014), suggesting that a modern representation has some bearing on the longer-term trends reflected in the accumulation record. However, variability in the forcing conditions over that period may also play an important role in the present clinoform structure. For example, the East Asian Monsoon intensity peaked between 8.6 and 7.7 kyr B.P., and then gradually decreased (Selvaraj et al., 2007). During the past few decades, due to global climate change, the East Asian Monsoon has experienced significant changes and both the winter and summer monsoon have weakened (Li et al., 2017; Tana et al., 2017). To fully understand the evolution of the clinoform development, multi-disciplinary studies of paleoclimate, sedimentation, and circulation at geological time scales are needed to address the variability in these climatic and anthropogenic factors.

7. Conclusion

In this paper, a high-resolution, coupled model of the Bohai and Yellow Seas is developed to investigate sediment transport and deposition processes in the region near a muddy deposit located at the tip of the Shandong Peninsula. The net sediment deposition over a full-year

model simulation has similar spatial patterns and rates as the longer-term accretion at the clinoform derived from the observations. The cross-shelf distribution of bed thickness changes is consistent with the seismic profiles of Yang and Liu (2007) with high accumulation rate in a focused region offshore and decreasing in the landward and seaward directions.

The model results indicate distinct seasonal variation in the sediment deposition patterns. From spring to autumn, a thermal front at the edge of the shelf favors sediment deposition in the clinoform region. Landward of the thermal front, the strong bottom shear stress and turbulent mixing result in greater SSC but minimal net deposition or net erosion. Seaward of the thermal front, stratification decreases the bottom shear stress and turbulence, and eventually suppuresses the sediment resuspension. The spatial differences in stratification, resuspension, and vertical mixing lead to a convergence in sediment transport and enhanced sediment deposition at the thermal front. Maximum sediment deposition occurs around the transition from summer to autumn, when the thermal front has shifted seaward but SSC in the coastal region has increased due to strengthening winds and waves. The combination of these processes – strong tidal currents and sediment resuspension along the shelf with trapping at the thermal front – make the structure and location of the sediment deposition that occurs during spring to autumn similar to net accumulation over the annual cycle, and similar to the longer-term accumulation associated with the omega-shaped clinoform with high accumulation rate in a focused region offshore and bidirectional decreasing. The seasonal shift of the thermal front seaward to deeper water induced by the seasonally varying surface net heat flux creates a broader depositional region, and this occurs in the region of the topset for the clinoform.

In winter, due to the stronger hydrodynamic forcing by winds and waves and the decrease in atmospheric heat input, the vertical mixing is significantly increased together with stratification destroyed, and the thermal front becomes weakened. As a result, bottom resuspension induces greater SSC and longshore sediment transport increases. Without trapping at the thermal front, net sediment deposition during

the winter decreases with distance across the shelf. Over the annual cycle, the net deposition patterns more closely reflect the enhanced deposition rates at the thermal front.

Acknowledgments

References

Alexander, C.R., DeMaster, D.J., Nittrouer, C.A., 1991. Sediment accumulation in a modern epicontinental-shelf setting: the Yellow Sea. Mar. Geol. 98 (1), 51–72.

Bao, X., Gao, G., Yan, J., 2001. Three dimensional simulation of tide and tidal current characteristics in the East China Sea. Oceanol. Acta 24 (2), 135–149.

Bai, H., Hu, D., Chen, Y., Wang, Q., 2004. Statistic characteristics of thermal structure in the southern Yellow Sea in summer. Chin. J. Oceanol. Limnol. 22 (3), 237–243.

Beardsley, R.C., Limeburner, R., Kim, K., Candela, J., 1992. Lagrangian flow observations in the East China, Yellow and Japan seas. La mer 30 (3), 297–314.

Bi, N., Yang, Z., Wang, H., Hu, B., Ji, Y., 2010. Sediment dispersion pattern off the present Huanghe (Yellow River) subdelta and its dynamic mechanism during normal river discharge period. Estuar. Coast Shelf Sci. 86 (3), 352–362.

Bi, N., Yang, Z., Wang, H., Fan, D., Sun, X., Lei, K., 2011. Seasonal variation of suspended-sediment transport through the southern Bohai Strait. Estuar. Coast Shelf Sci. 93 (3), 239–247.

Bian, C., Jiang, W., Greatbatch, R.J., 2013a. An exploratory model study of sediment transport sources and deposits in the Bohai Sea, Yellow Sea, and East China Sea. J. Geophys. Res.: Oceans 118 (11), 5908–5923.

Bian, C., Jiang, W., Quan, Q., Wang, T., Greatbatch, R.J., Li, W., 2013b. Distributions of suspended sediment concentration in the Yellow Sea and the East China Sea based on field surveys during the four seasons of 2011. J. Mar. Syst. 121, 24–35.

Booij, N.R.R.C., Ris, R.C., Holthuijsen, L.H., 1999. A third-generation wave model for coastal regions: 1. Model description and validation. J. Geophys. Res.: Oceans 104 (C4), 7649–7666.

Chen, G.G., Zhai, F.G., Li, P.L., Liu, X., 2016. Numberical study of wave height seasonality in the Yellow Sea. Mar. Sci. 40 (11), 155–168 (in Chinese with English abstract).

Chen, Q., Zhu, Y., 2012. Holocene evolution of bottom sediment distribution on the continental shelves of the Bohai Sea, Yellow Sea and east China sea. Sediment. Geol. 273, 58–72.

Chen, Z., Song, B., Wang, Z., Cai, Y., 2000. Late Quaternary evolution of the sub-aqueous Yangtze Delta, China: sedimentation, stratigraphy, palynology, and deformation. Mar. Geol. 162 (2–4), 423–441.

Choi, B.H., Eum, H.M., Woo, S.B., 2003. A synchronously coupled tide–wave–surge model of the Yellow Sea. Coast Eng. 47 (4), 381–398.

Chu, P.C., Fralick Jr., C.R., Haeger, S.D., Carron, M.J., 1997. A parametric model for the Yellow Sea thermal variability. J. Geophys. Res.: Oceans 102 (C5), 10499–10507.

Editorial Board for Marine Atlas, 1992. Marine Atlas of Bohai Sea, Yellow Sea, East China Sea: Hydrology. China Ocean Press, Beijing.

Egbert, G.D., Bennett, A.F., Foreman, M.G., 1994. TOPEX/POSEIDON tides estimated using a global inverse model. J. Geophys. Res.: Oceans 99 (C12), 24821–24852.

Egbert, G.D., Erofeeva, S.Y., 2002. Efficient inverse modeling of barotropic ocean tides. J. Atmos. Ocean. Technol. 19 (2), 183–204.

Fairall, C.W., Bradley, E.F., Hare, J.E., Grachev, A.A., Edson, J.B., 2003. Bulk parameterization of air–sea fluxes: updates and verification for the COARE algorithm. J. Clim. 16 (4), 571–591.

Fang, G., 1986. Tide and tidal current charts for the marginal seas and adjacent to China. Chin. J. Oceanol. Limnol. 4 (1), 1–16.

Geyer, W.R., 1993. The importance of suppression of turbulence by stratification on the estuarine turbidity maximum. Estuaries 16 (1), 113–125.

Hickox, R., Belkin, I., Cornillon, P., Shan, Z., 2000. Climatology and seasonal variability of ocean fronts in the East China, Yellow and Bohai Seas from satellite SST data. Geophys. Res. Lett. 27 (18), 2945–2948.

Hsueh, Y., 1988. Recent current observations in the eastern Yellow Sea. J. Geophys. Res.: Oceans 93 (C6), 6875–6884.

Ichikawa, H., Beardsley, R.C., 2002. The current system in the yellow and east China seas. J. Oceanogr. 58 (1), 77–92.

Isobe, A., 2008. Recent advances in ocean-circulation research on the Yellow Sea and east China sea shelves. J. Oceanogr. 64 (4), 569–584.

Jacob, R., Larson, J., Ong, E., 2005. M × N communication and parallel interpolation in Community Climate System Model Version 3 using the model coupling toolkit. Int. J. High Perform. Comput. Appl. 19 (3), 293–307.

Jerlov, N.G., 1968. Optical Oceanography. American Elsevier Publ. Co. Inc., New York.

Jiang, W., Pohlmann, T., Sündermann, J., Feng, S., 2000. A modelling study of SPM transport in the Bohai Sea. J. Mar. Syst. 24 (3–4), 175–200.

Kuehl, S.A., DeMaster, D.J., Nittrouer, C.A., 1986. Nature of sediment accumulation on the Amazon continental shelf. Cont. Shelf Res. 6 (1–2), 209–225.

Larson, J., Jacob, R., Ong, E., 2005. The model coupling toolkit: a new Fortran90 toolkit for building multiphysics parallel coupled models. Int. J. High Perform. Comput. Appl. 19 (3), 277–292.

Lee, H.J., Chough, S.K., 1989. Sediment distribution, dispersal and budget in the Yellow Sea. Mar. Geol. 87 (2–4), 195–205.

Li, G., Li, P., Liu, Y., Qiao, L., Ma, Y., Xu, J., Yang, Z., 2014. Sedimentary system response to the global sea level change in the East China Seas since the last glacial maximum. Earth Sci. Rev. 139, 390–405.

Li, G., Wang, H., Liao, H., 2010. Numerical simulation on seasonal transport variations and mechanisms of suspended sediment discharged from the Yellow River to the Bohai Sea. J. Geogr. Sci. 20 (6), 923–937.

Li, G., Yang, Z., Liu, Y., 2005. Formation Environment of the Seafloor Sediment in the East China Sea. Science Press, Beijing.

Li, H., Yuan, Y., 1992. On the formation and maintenance mechanisms of the cold water mass of the yellow sea. Chin. J. Oceanol. Limnol. 10 (2), 97–106.

Li, J., Li, G., Xu, J., Dong, P., Qiao, L., Liu, S., Sun, P., Fan, Z., 2016. Seasonal evolution of the Yellow Sea cold water mass and its interactions with ambient hydrodynamic system. J. Geophys. Res.: Oceans 121 (9), 6779–6792.

Li, X., Cheng, H., Tan, L., Ban, F., Sinha, A., Duan, W., Li, H., Zhang, H., Ning, Y., Kathayat, G., Edwards, R.L., 2017. The East Asian summer monsoon variability over the last 145 years inferred from the Shihua Cave record, North China. Sci. Rep. 7 (1), 7078.

Lie, H.J., Cho, C.H., 1994. On the origin of the tsushima warm current. J. Geophys. Res.: Oceans 99 (C12), 25081–25091.

Lie, H.J., Cho, C.H., Lee, S., 2009. Tongue-shaped frontal structure and warm water intrusion in the southern Yellow Sea in winter. J. Geophys. Res.: Oceans 114 (C01003).

Lin, S., Zou, T., Gao, H., Guo, X., 2009. The vertical attenuation of irradiance as a function of turbidity: a case of the Huanghai (Yellow) Sea in spring. Acta Oceanol. Sin. 28 (5), 66–75.

Lin, X., Yang, J., 2011. An asymmetric upwind flow, Yellow Sea Warm Current: 2. Arrested topographic waves in response to the northwesterly wind. J. Geophys. Res.: Oceans 116 (C4).

Liu, C., Sui, J., He, Y., Hirshfield, F., 2013. Changes in runoff and sediment load from major Chinese rivers to the Pacific Ocean over the period 1955-2010. Int. J. Sediment Res. 28 (4), 486–495.

Liu, J., Saito, Y., Wang, H., Yang, Z., Nakashima, R., 2007a. Sedimentary evolution of the holocene subaqueous clinoform off the Shandong Peninsula in the Yellow Sea. Mar. Geol. 236 (3–4), 165–187.

Liu, J.P., DeMaster, D.J., Nguyen, T.T., Saito, Y., Nguyen, V.L., Ta, T.K.O., Li, X., 2017. Stratigraphic formation of the Mekong River Delta and its recent shoreline changes. Oceanography 30 (3), 72–83.

Liu, J.P., Li, A.C., Xu, K.H., Velozzi, D.M., Yang, Z.S., Milliman, J.D., DeMaster, D.J., 2006. Sedimentary features of the Yangtze River-derived along-shelf clinoform deposit in the east China sea. Cont. Shelf Res. 26 (17–18), 2141–2156.

Liu, J.P., Milliman, J.D., Gao, S., 2002. The Shandong mud wedge and post-glacial sediment accumulation in the Yellow Sea. Geo Mar. Lett. 21 (4), 212–218.

Liu, J.P., Milliman, J.D., Gao, S., Cheng, P., 2004. Holocene development of the Yellow River's subaqueous delta, north Yellow Sea. Mar. Geol. 209 (1–4), 45–67.

Liu, J., Saito, Y., Kong, X., Wang, H., Xiang, L., Wen, C., Nakashima, R., 2010. Sedimentary record of environmental evolution off the Yangtze River estuary, East China Sea, during the last ~ 13,000 years, with special reference to the influence of the Yellow River on the Yangtze River delta during the last 600 years. Quat. Sci. Rev. 29 (17–18), 2424–2438.

Liu, J.P., Xu, K.H., Li, A.E.A., Milliman, J.D., Velozzi, D.M., Xiao, S.B., Yang, Z.S., 2007b. Flux and fate of Yangtze River sediment delivered to the east China sea. Geomorphology 85 (3–4), 208–224.

Lu, J., Qiao, F.L., Wang, X.H., Wang, Y.G., Teng, Y., Xia, C.S., 2011. A numerical study of transport dynamics and seasonal variability of the Yellow River sediment in the Bohai and Yellow seas. Estuar. Coast Shelf Sci. 95 (1), 39–51.

Luo, Z., Zhu, J., Wu, H., Li, X., 2017. Dynamics of the sediment plume over the Yangtze bank in the yellow and east China seas. J. Geophys. Res.: Oceans 122 (12), 10073–10090.

Ma, J., Qiao, F., Xia, C., Kim, C.S., 2006. Effects of the Yellow Sea Warm Current on the winter temperature distribution in a numerical model. J. Geophys. Res.: Oceans 111 (C11S04).

Madsen, O.S., 1994. Spectral wave–current bottom boundary layer flows. In: Coastal Engineering 1994. Proceedings of the 24th International Conference on Coastal Engineering Research Council, Kobe, Japan, pp. 384–398.

Martin, J.M., Zhang, J., Shi, M.C., Zhou, Q., 1993. Actual flux of the huanghe (Yellow River) sediment to the western pacific ocean. Neth. J. Sea Res. 31 (3), 243–254.

Milliman, J.D., Meade, R.H., 1983. World-wide delivery of river sediment to the oceans. J. Geol. 91 (1), 1–21.

Milliman, J.D., Syvitski, J.P., 1992. Geomorphic/tectonic control of sediment discharge to the ocean: the importance of small mountainous rivers. J. Geol. 100 (5), 525–544.

Milliman, J.D., Yun-Shan, Q., Mei-e, R., Saito, Y., 1987. Man's influence on the erosion and transport of sediment by Asian rivers: the Yellow River (Huanghe) example. J. Geol. 95 (6), 751–762.

Moon, J.H., Hirose, N., Yoon, J.H., 2009. Comparison of wind and tidal contributions to seasonal circulation of the Yellow Sea. J. Geophys. Res.: Oceans 114 (C8).

Mountain, D.G., Taylor, M.H., 1996. Fluorescence structure in the region of the tidal mixing front on the southern flank of Georges Bank. Deep Sea Res. Part II Top. Stud. Oceanogr. 43 (7–8), 1831–1853.

Murphy, A.H., 1988. Skill scores based on the mean square error and their relationships to

the correlation coefficient. Mon. Weather Rev. 116 (12), 2417–2424.

Naimie, C.E., Blain, C.A., Lynch, D.R., 2001. Seasonal mean circulation in the Yellow Sea—a model-generated climatology. Cont. Shelf Res. 21 (6–7), 667–695.

Nittrouer, C.A., Curtin, T.B., DeMaster, D.J., 1986. Concentration and flux of suspended sediment on the Amazon continental shelf. Cont. Shelf Res. 6 (1–2), 151–174.

Nittrouer, C.A., Kuehl, S.A., Figueiredo, A.G., Allison, M.A., Sommerfield, C.K., Rine, J.M., Faria, L.Z., Silveira, O.M., 1996. The geological record preserved by Amazon shelf sedimentation. Cont. Shelf Res. 16 (5–6), 817–841.

Oost, W.A., Komen, G.J., Jacobs, C.M.J., Van Oort, C., 2002. New evidence for a relation between wind stress and wave age from measurements during ASGAMAGE. Boundary-Layer Meteorol. 103 (3), 409–438.

Pan, H., 1993. Analysis of the stratification features of the Yellow Sea and the location of its general shelf front in the warm half-year. Chin. J. Oceanol. Limnol. 11 (1), 80–88.

Pang, C., Liang, J., Hu, D., Wang, F., Chen, Y., Bai, H., Bai, X., 2004. Surface circulation patterns observed by drifters in the Yellow Sea in summer of 2001, 2002 and 2003. Chin. J. Oceanol. Limnol. 22 (3), 209–216.

Park, Y.H., 1986. A simple theoretical model for the upwind flow in the southern Yellow Sea. J. Oceanol. Soc. Korea 21 (4), 203–210.

Qiao, L., Zhong, Y., Wang, N., Zhao, K., Huang, L., Wang, Z., 2016. Seasonal transportation and deposition of the suspended sediments in the Bohai Sea and Yellow Sea and the related mechanisms. Ocean Dynam. 66 (5), 751–766.

Qiao, S., Shi, X., Wang, G., Zhou, L., Hu, B., Hu, L., Yang, G., Liu, Y., Yao, Z., Liu, S., 2017. Sediment accumulation and budget in the Bohai Sea, Yellow Sea and east China sea. Mar. Geol. 390, 270–281.

Qin, Y.S., Li, F., 1983. Study of influence of sediment loads discharged from Huanghai Sea. In: Proceedings International Symposium on Sedimentation on the Continental Shelf with Special Reference to the East China Sea (I). Hangzhou, China. China, pp. 91–101.

Qu, L., Lin, X., Hetland, R.D., Guo, J., 2018. The asymmetric continental shelf wave in response to the synoptic wind burst in a semienclosed double-shelf basin. J. Geophys. Res.: Oceans 123 (1), 131–148.

Ralston, D.K., Geyer, W.R., Lerczak, J.A., 2010. Structure, variability, and salt flux in a strongly forced salt wedge estuary. J. Geophys. Res.: Oceans 115 (C6).

Ren, S., Xie, J., Zhu, J., 2014. The roles of different mechanisms related to the tide-induced fronts in the Yellow Sea in summer. Adv. Atmos. Sci. 31 (5), 1079–1089.

Riedlinger, S.K., Jacobs, G.A., 2000. Study of the dynamics of wind-driven transports into the Yellow Sea during winter. J. Geophys. Res.: Oceans 105 (C12), 28695–28708.

Selvaraj, K., Chen, C.T.A., Lou, J.Y., 2007. Holocene East Asian monsoon variability: links to solar and tropical Pacific forcing. Geophys. Res. Lett. 34 (1).

Shchepetkin, A.F., McWilliams, J.C., 2005. The regional oceanic modeling system (ROMS): a split-explicit, free-surface, topography-following-coordinate oceanic model. Ocean Model. 9 (4), 347–404.

Simpson, J.H., Bowers, D., 1981. Models of stratification and frontal movement in shelf seas. Deep Sea Research Part A. Oceanographic Research Papers 28 (7), 727–738.

Simpson, J.H., Hunter, J.R., 1974. Fronts in the Irish sea. Nature 250 (5465), 404.

Su, J.L., Yuan, Y.L., 2005. China Offshore Hydrology. China Ocean Press, Beijing, pp. 1–192 (in Chinese).

Tana, Fang, Y., Liu, B., Sun, S., Wang, H., 2017. Dramatic weakening of the ear-shaped thermal front in the Yellow Sea during 1950s–1990s. Acta Oceanol. Sin. 36 (5), 51–56.

Taylor, P.K., Yelland, M.J., 2001. The dependence of sea surface roughness on the height and steepness of the waves. J. Phys. Oceanogr. 31 (2), 572–590.

Teague, W.J., Jacobs, G.A., 2000. Current observations on the development of the Yellow Sea warm current. J. Geophys. Res.: Oceans 105 (C2), 3401–3411.

Teague, W.J., Perkins, H.T., Hallock, Z.R., Jacobs, G.A., 1998. Current and tide observations in the southern yellow sea. Journal of Geophysical Research Oceans 103 (C12), 27783–27793.

Wang, A., Wang, H., Bi, N., Wu, X., 2016. Sediment transport and dispersal pattern from the Bohai Sea to the Yellow Sea. J. Coast. Res. 74 (sp1), 104–116.

Wang, B., Hirose, N., Kang, B., Takayama, K., 2014a. Seasonal migration of the Yellow Sea bottom cold water. J. Geophys. Res.: Ocean 119, 4430–4443.

Wang, F., Liu, C., 2009. An N-shape thermal front in the western South Yellow Sea in winter. Chin. J. Oceanol. Limnol. 27 (4), 898–906.

Wang, H., Saito, Y., Zhang, Y., Bi, N., Sun, X., Yang, Z., 2011. Recent changes of sediment flux to the western Pacific Ocean from major rivers in East and Southeast Asia. Earth Sci. Rev. 108 (1–2), 80–100.

Wang, H., Wang, A., Bi, N., Zeng, X., Xiao, H., 2014b. Seasonal distribution of suspended sediment in the Bohai Sea, China. Cont. Shelf Res. 90, 17–32.

Wang, H., Wu, X., Bi, N., Li, S., Yuan, P., Wang, A., Syvitski, J., Saito, Y., Yang, Z., Liu, S., Nittrouer, J., 2017. Impacts of the dam-orientated water-sediment regulation scheme

on the lower reaches and delta of the Yellow river (huanghe): a review. Glob. Planet. Chang. 127, 93–113.

Wang, H., Yang, Z., Saito, Y., Liu, J.P., Sun, X., Wang, Y., 2007. Stepwise decreases of the Huanghe (Yellow River) sediment load (1950–2005): impacts of climate change and human activities. Glob. Planet. Chang. 57 (3–4), 331–354.

Wang, R., Zhang, Y., Xie, F., Zhao, S., 2012. Grain size distribution and transportation trends of bottom sediments in the sand ridge field of the south Yellow Sea, China. Mar. Geol. Quat. Geol. 32 (6), 1–7 (in Chinese with English abstract).

Wang, Y., Qiao, L., Yang, Z., Bao, X., Zhao, M., Wang, G., 2013. Suspended sediment transport and deposition due to strong regional shear current front: an example from the shelf waters off eastern Shandong Peninsula. Acta Sedimentol. Sin. 31 (3), 486–496 (in Chinese with English abstract).

Warner, J.C., Armstrong, B., He, R., Zambon, J.B., 2010. Development of a coupled ocean–atmosphere–wave–sediment transport (COAWST) modeling system. Ocean Model. 35 (3), 230–244.

Warner, J.C., Sherwood, C.R., Arango, H.G., Signell, R.P., 2005. Performance of four turbulence closure models implemented using a generic length scale method. Ocean Model. 8 (1–2), 81–113.

Warner, J.C., Sherwood, C.R., Signell, R.P., Harris, C.K., Arango, H.G., 2008. Development of a three-dimensional, regional, coupled wave, current, and sediment-transport model. Comput. Geosci. 34 (10), 1284–1306.

Wright, L.D., Nittrouer, C.A., 1995. Dispersal of river sediments in coastal seas: six contrasting cases. Estuaries 18 (3), 494–508.

Wu, H., Gu, J., Zhu, P., 2018. Winter counter-wind transport in the inner southwestern Yellow Sea. J. Geophys. Res.: Oceans 123 (1), 411–436.

Wu, H., Zhu, J., 2010. Advection scheme with 3rd high-order spatial interpolation at the middle temporal level and its application to saltwater intrusion in the Changjiang Estuary. Ocean Model. 33 (1–2), 33–51.

Xia, C., Qiao, F., Yang, Y., Ma, J., Yuan, Y., 2006. Three-dimensional structure of the summertime circulation in the Yellow Sea from a wave-tide-circulation coupled model. J. Geophys. Res.: Oceans 111 (C11).

Xu, D., Yuan, Y., Liu, Y., 2003. The baroclinic circulation structure of Yellow Sea cold water mass. Sci. China Earth Sci. 46 (2), 117–126.

Xu, G., Liu, J., Pei, S., Gao, M., Kong, X., 2016. Transport pathway and depocenter of anthropogenic heavy metals off the Shandong Peninsula, China. Estuarine. Coastal and Shelf Science 180, 168–178.

Xu, K., Li, A., Liu, J.P., Milliman, J.D., Yang, Z., Liu, C.S., Kao, S.J., Wan, S., Xu, F., 2012. Provenance, structure, and formation of the mud wedge along inner continental shelf of the East China Sea: a synthesis of the Yangtze dispersal system. Mar. Geol. 291, 176–191.

Xu, K., Milliman, J.D., Li, A., Liu, J.P., Kao, S.J., Wan, S., 2009. Yangtze-and taiwan-derived sediments on the inner shelf of east China sea. Cont. Shelf Res. 29 (18), 2240–2256.

Xue, C., 1993. Historical changes in the Yellow River delta, China. Mar. Geol. 113 (3–4), 321–330.

Yang, S.Y., Jung, H.S., Lim, D.I., Li, C.X., 2003. A review on the provenance discrimination of sediments in the Yellow Sea. Earth Sci. Rev. 63 (1–2), 93–120.

Yang, Z.S., Liu, J.P., 2007. A unique Yellow River-derived distal subaqueous delta in the Yellow Sea. Mar. Geol. 240 (1–4), 169–176.

Yuan, P., 2015. Distribution of Surface Sediment in the Bohai Sea and its Relationship with Sediment Supply and Sedimentary Dynamic Environment. Ocean University of China (in Chinese with English abstract).

Zang, Z., Xue, Z.G., Bi, N., Yao, Z., Wu, X., Ge, Q., Wang, H., 2017. Seasonal and intra-seasonal variations of suspended-sediment distribution in the Yellow Sea. Cont. Shelf Res. 148, 116–129.

Zeng, X., He, R., Xue, Z., Wang, H., Wang, Y., Yao, Z., Guan, W., Warrillow, J., 2015. River-derived sediment suspension and transport in the Bohai, Yellow, and East China Seas: a preliminary modeling study. Cont. Shelf Res. 111, 112–125.

Zhang, S.W., Wang, Q.Y., Lü, Y., Cui, H., Yuan, Y.L., 2008. Observation of the seasonal evolution of the Yellow Sea cold water mass in 1996–1998. Cont. Shelf Res. 28 (3), 442–457.

Zhao, B., 1985. The fronts of the Huanghai Sea cold water mass induced by tidal mixing. Oceanol. Limnol. Sinica 16, 451–459.

Zhao, B., 1987. A preliminary study of continental shelf fronts in the western part of southern Huanghai Sea and circulation structure in the front region of the Huanghai Cold Water Mass (HCWM). Oceanol. Limnol. Sinica 18, 217–226 (in Chinese, with English abstract).

Zong, Y., 2004. Mid-holocene sea-level highstand along the southeast coast of China. Quat. Int. 117 (1), 55–67.